

IRAC2 at the 2.2-m Telescope

A. MOORWOOD, G. FINGER, P. BIEREICHEL, B. DELABRE, A. VAN DIJSSELDONK,
G. HUSTER, J.-L. LIZON, M. MEYER, ESO, Garching,
H. GEMPERLEIN, A. MONETI, ESO, La Silla

ESO's new infrared camera, IRAC2, is equipped with a Rockwell 256×256 pixel NICMOS3 array for imaging through broad and narrow band filters between 1 and 2.5 μm and a K (2.2 μm) band scanning Fabry Perot. A preview of some of its capabilities was already given in the June 1992 issue of the *Messenger* (68, 42) where we showed a 2.1 μm broad band image of a $z = 0.2$ galaxy cluster and a narrow band [FeII](1.64 μm) mosaic image of the SNR RCW103 obtained during the first test on the 2.2-m telescope in May. In this article we give a description of the instrument and its observing modes together with performance figures derived from the test data and some additional images selected to illustrate some of its possible scientific applications.

1. Description of IRAC2

Figure 1 is a photograph of IRAC2 mounted on the F/35 infrared adapter at the Cassegrain focus of the 2.2-m telescope. The camera itself is housed in a modified Oxford Instruments 4-l liquid helium cryostat which is partially hidden by the attached motor control and detector acquisition electronics. (Although the NICMOS3 array has a long wavelength cut-off at $\sim 2.5 \mu\text{m}$ and requires cooling to only $\sim 60\text{K}$ using pumped liquid nitrogen, a He cryostat was selected in order to keep open the possibility of installing arrays operating out to 5 μm in the same camera in the future.) The black unit sandwiched between the camera and the adapter houses the scanning Fabry Perot etalon(s) and remotely controlled exchange mechanism used to rotate it in front of the entrance window.

Figure 2 shows the layout of the camera optics. The input doublet field lens, which also acts as the cryostat entrance window, provides for a 70-mm diameter (~ 3 arcmin.) field and re-images the telescope pupil at the cold 4.5-mm diameter cold stop just behind a 24-position filter wheel. The field is re-imaged on the detector by one of the five remotely selectable objectives mounted on a wheel. In order to minimize flexure, the camera itself is rigidly attached to the outer vacuum housing via glass thermal isolators and the optics and detector mount are cooled via thermal connections to the inner radiation shield and

inner cryogen tank respectively. Figure 3 is a photograph of the cooled optical assembly showing the filter wheel on the left and, on the right, the objective wheel which is largely hidden by the detector mount.

The NICMOS3 array is a hybrid device consisting of a HgCdTe diode array bonded via indium bumps to a multi-

plexer which is structured in four quadrants having separate output amplifiers. It is controlled and read by a programmable, VME-based, detector controller which has been developed in Garching and contains four A/D converters allowing simultaneous reading of the four quadrants. This system also contains a Motorola 68030 processor which runs



Figure 1: IRAC2 mounted on the F/35 adapter at the 2.2-m telescope.

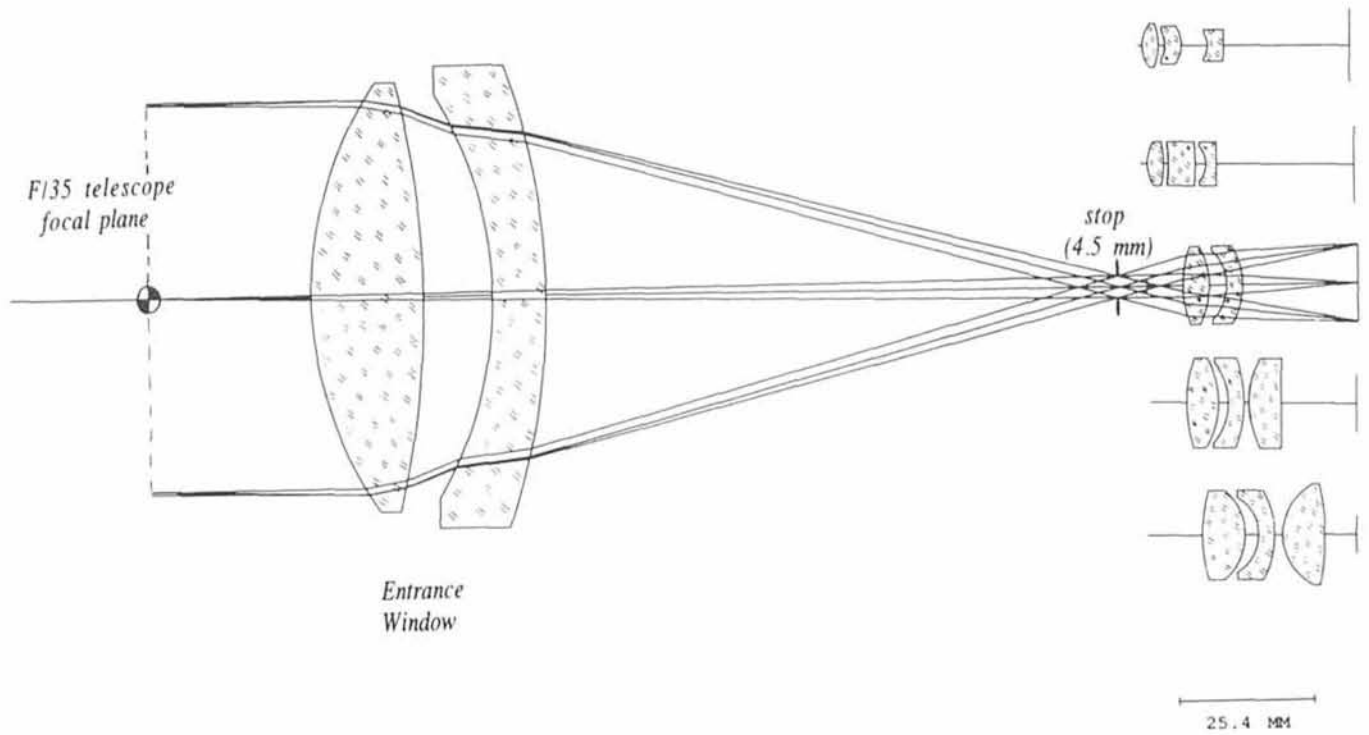


Figure 2: Optical layout of the camera. The input doublet covers a 70-mm (3-arcmin.) diameter field and acts both as the field lens and the cryostat window. A 24 position filter wheel (not shown) is located in front of the cold pupil stop and the five remotely interchangeable objectives mounted on a wheel behind the pupil stop provide for magnifications from ~ 0.14 – $1.1''/\text{pixel}$.

detector pre-processing software under the OS9 operating system. This processor receives command files specifying the required detector set-up from the instrument workstation; transmits real time images to a monitor in the control room and sends images, with or without co-averaging, to the instrument workstation. The real time display is particularly useful during set-up on an object field as pixel values and coordinates can be measured and cut-levels set using only the mouse. The observer can select from a variety of read-out modes including double and triple correlated and multiple nondestructive sampling. A novel variant of the latter mode, tested in May but not yet implemented in a very user friendly way, also achieves partial seeing correction by tracking a reference object in the field and applying a shift and add algorithm to each non-destructively read sub-image before solution of the error equations for the integration ramps. At present, the minimum time required to read out a full 256×256 image is ~ 700 ms. A faster read-out could improve the performance of the real time shift and add mode and could be implemented in the future by installing a faster pre-processor which is now available.

In view of the plan to phase out the HP 1000 series computers on La Silla the user interface runs on a workstation and MIDAS is used on-line for data storage, image display and quick-look anal-

ysis. The arrangement used during the test is shown in Figure 4 but is provisional pending completion of a new standard user interface and VME based motor control system on La Silla. Instrument set-up and control is via typed commands and menu bars on the

HP370 which runs control software written in Basic which was developed originally only for laboratory testing in Garching. This workstation is connected to the instrument via CAMAC for the motor controls, a GPIB bus for the Fabry Perot control and ethernet fibre optics

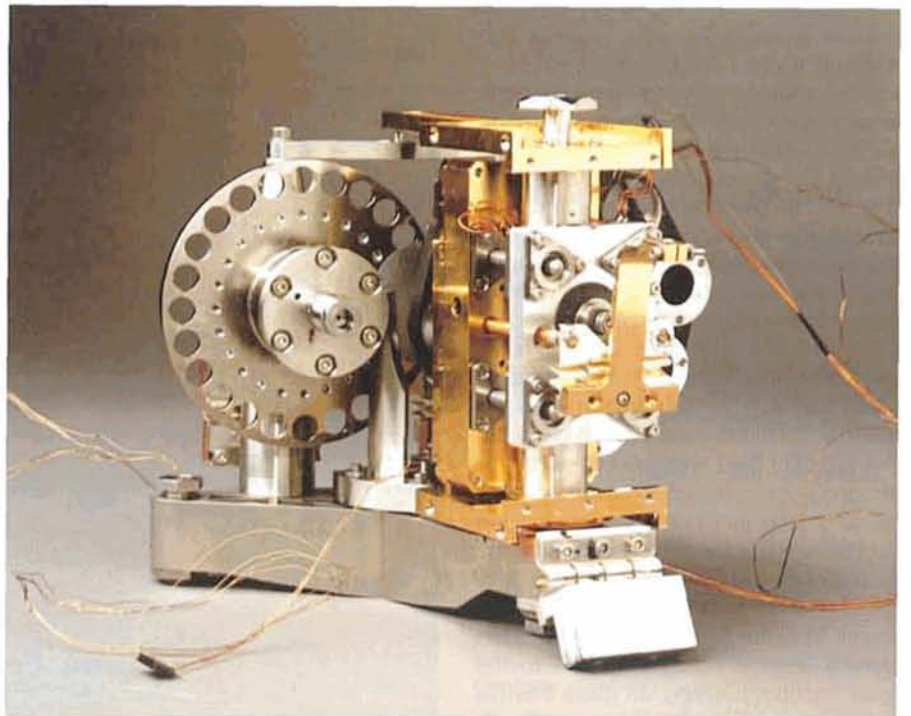


Figure 3: The cryogenic optical assembly showing the filter wheel on the left and the objective wheel on the right which is partially hidden by the detector mount.

links to the detector pre-processor. There is also an RS232 link to the HP1000 telescope computer which is used to step the secondary mirror during focus exposures and to read coordinates which are written in the file headers. The HP730 workstation is used to run two parallel MIDAS sessions. One of these is set in the background mode and is used to display images (with or without background subtraction as requested) and store them in the correct format while the other is available for interactive image analysis using MIDAS. The HP370 should become superfluous once the new user interface is available when both the control software and MIDAS will run on the HP730 with a separate X11 window terminal available for on-line analysis.

2. Observing Modes

IRAC2 provides for imaging at a variety of image scales through broad and narrow band filters between 1 and 2.5 μm and a K(2.2 μm) band scanning Fabry Perot etalon yielding $R \sim 1000$.

The available filters, image scales and corresponding field sizes are summarized in Table 1. The scales A-D are measured values derived from images of astrometric double stars. Although objectives D and E should provide a circular 3' field limited by the entrance window this is slightly vignetted on two sides at present by the dichroic mirror in the F/35 adapter. For broad-band imaging, when background noise dominates, it is recommended in any case to use objective C (0.494"/pix.) in general. This objective has the highest efficiency, yields the maximum square field and provides reasonable sampling under average seeing conditions. Objective B(0.27"/pix.) can be used when better sampling/spatial resolution is more important than field.

The desired observing mode, filter, magnification and detector parameters are set via the workstation user interface. A present, the standard modes are (i) focus (ii) DC observing (staring) and (iii) Fabry Perot scan. Chopping and automatic beamswitching could be implemented but are not considered particularly useful with this array. Real time shift and add is more complicated to set-up and is not yet available as a standard mode.

For focussing on a star the focus mode is used to automatically step the telescope secondary mirror through a specified range of positions and record images which are displayed in a line at the end of the measurement. The best focus can then be determined by measuring the FWHM using MIDAS and the secondary set to that position. Dif-

Table 1: IRAC2 characteristics.

| Image Scales and Fields | | |
|-------------------------|-----------------------------|-----------------------------------|
| Objective | Arcsec/pix | Arcsec |
| A | 0.14 | 36×36 |
| B | 0.27 | 69×69 |
| C | 0.49 | 125×125 |
| D | 0.70 | $\Phi = 180$ |
| E | 1.1 | $\Phi = 180$ |
| Filters | | |
| Name | λ (μm) | $\Delta\lambda$ (μm) |
| J | 1.25 | 0.3 |
| H | 1.65 | 0.3 |
| K' | 2.1 | 0.34 |
| K | 2.2 | 0.4 |
| NB1 (FeII) | 1.262 | 0.04 |
| NB2 (FeII) | 1.645 | 0.04 |
| NB3 (HeI) | 2.058 | 0.036 |
| NB4 | 2.105 | 0.037 |
| NB5 (H ₂) | 2.121 | 0.039 |
| NB6 | 2.136 | 0.038 |
| NB7 | 2.148 | 0.037 |
| NB8 (Br γ) | 2.164 | 0.037 |
| NB9 | 2.177 | 0.038 |
| NB10 | 2.216 | 0.075 |
| NB11 (CO) | 2.365 | 0.088 |
| Fabry Perot | $\sim 2-2.5$ | $\lambda/\Delta\lambda \sim 1000$ |

ferential focus changes during the night due to telescope temperature changes can be made using a calibration curve without needing to repeat the star measurements. A focus shift is required when using the Fabry Perot.

The DC mode used for observing requires little explanation. Each image is written into a separate file with its own identifier and a header which contains all the instrument and detector parameters plus the time and telescope coordinates.

In the Fabry Perot mode the required narrow band order isolating filter can be set manually or automatically and both the filter transmission curve and the wavelengths corresponding to the different orders displayed on the screen. A sequence of images can be made by entering a list of the desired

wavelengths which are automatically written in the file headers.

The detector set-up includes selection of the read mode; the on-chip integration time (DIT); the number of integrations (NDIT) to be averaged in the pre-processor before transmission to the workstation and the number of such measurements to be made (cycles) and stored in separate files. If in doubt, the read-mode should be set to double-correlated. Multiple, non-destructive, sampling is needed for the shift and add mode and yields somewhat lower read-noise for long measurements but involves larger time overheads and increases the amplifier glow in the corners of the array. The main considerations in selecting DIT are that it should be short enough to avoid saturation ($K \sim 8$ for DIT = 1s with objective C) but long enough

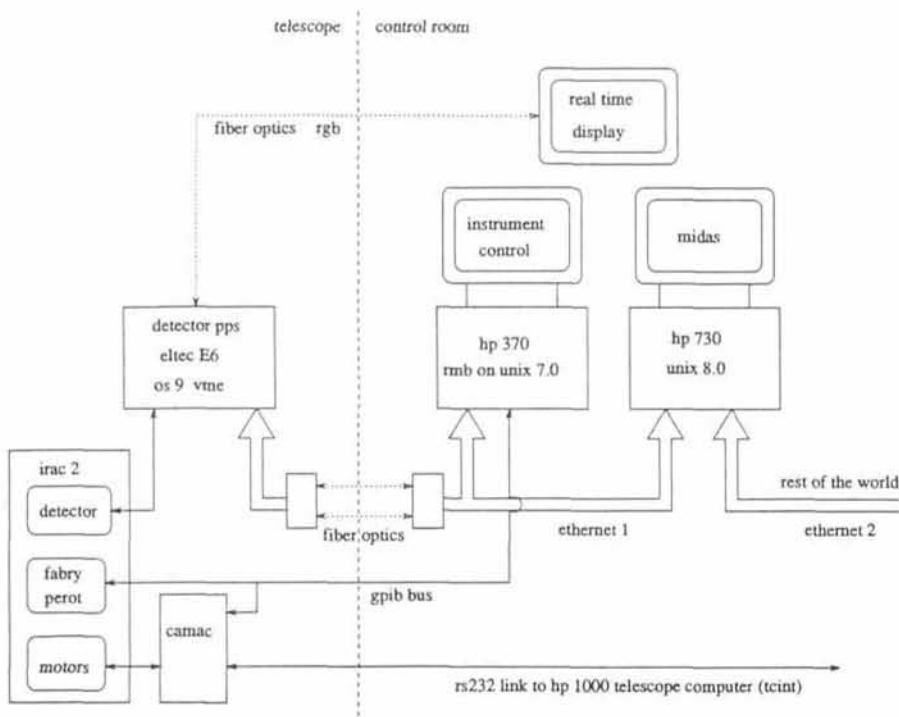


Figure 4: Provisional control set-up for the IRAC2 test in May.

to achieve background limited performance when observing faint sources (typically a few seconds for the broadband filters). Most of the test observations were made using $DIT = 1s$ for standard stars and 10–30s for the science frames. The value of NDIT is a trade-off between the s/n ratio in each stored image and the time between object and sky frames which should not be too long because of sky fluctuations. During the test NDIT was selected typically such that $DIT \times NDIT$ was 2–5 min and $CYCLES = 1$. In order to remove stars and achieve optimal sky subtraction it is, in any case, necessary to have several sky frames on different positions. For the optimal removal of bad pixels it is also desirable to have several object frames on different positions. Particularly for faint sources therefore the best observing procedure is to combine all requirements by making a series of exposures at telescope positions separated by 10–20 arcsec. on the sky. All frames can then be used to derive the mean sky with the stars removed and, after re-registering, be combined into a final object image in which bad pixels have been replaced with good ones from other frames in the stack. This technique was used to produce the galaxy cluster image reproduced in the June 1992 *Messenger*. An alternative, used for several of the test images reproduced here, is to use the same object position but different sky positions or, in the limit, just single object and sky frames. This simplifies the data reduction (particularly the on-line quick look

analysis) but means that only half the total time is spent on the object and bad pixels can only be corrected within the image by median filtering or pixel inter-

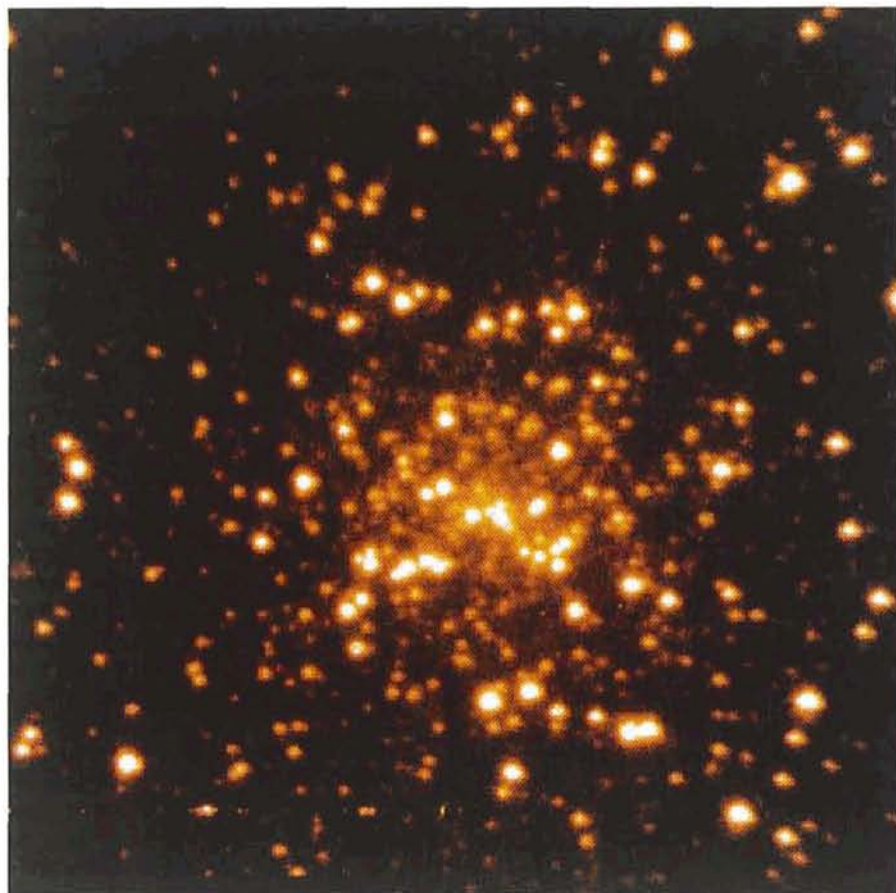


Figure 5: K band image of the core of the globular cluster M15. Integration time was 60s (30×2s) on object and sky and the scale is 0.27"/pixel.

polation/replacement using a bad pixel mask.

3. Performance

Characteristics of the presently installed NICMOS3 array are summarized in Table 2 and the overall broad band system performance as measured on the telescope is given in Table 3.

The magnitude limits obtained in the broad band filters correspond to the background limits expected from the measured counts and for longer measurement times the s/n should improve as $t^{1/2}$. In K' , for example, the limit in 20 min should be 19.6 mag/(arcsec²) while the value derived from the galaxy cluster image shown in the June *Messenger* is 19.8, i.e. actually somewhat better than expected but probably consistent within the uncertainties (e.g. the detector electrons/ADU conversion factor).

Good photometry should be possible with this camera. Zero points determined from standard stars observed over the 7 nights (when the sky was clear) agree to within 1–2% after flat fielding. The flat fields used were obtained by taking difference images of the diffusing screen in the dome with the halogen lamp on and off. This technique

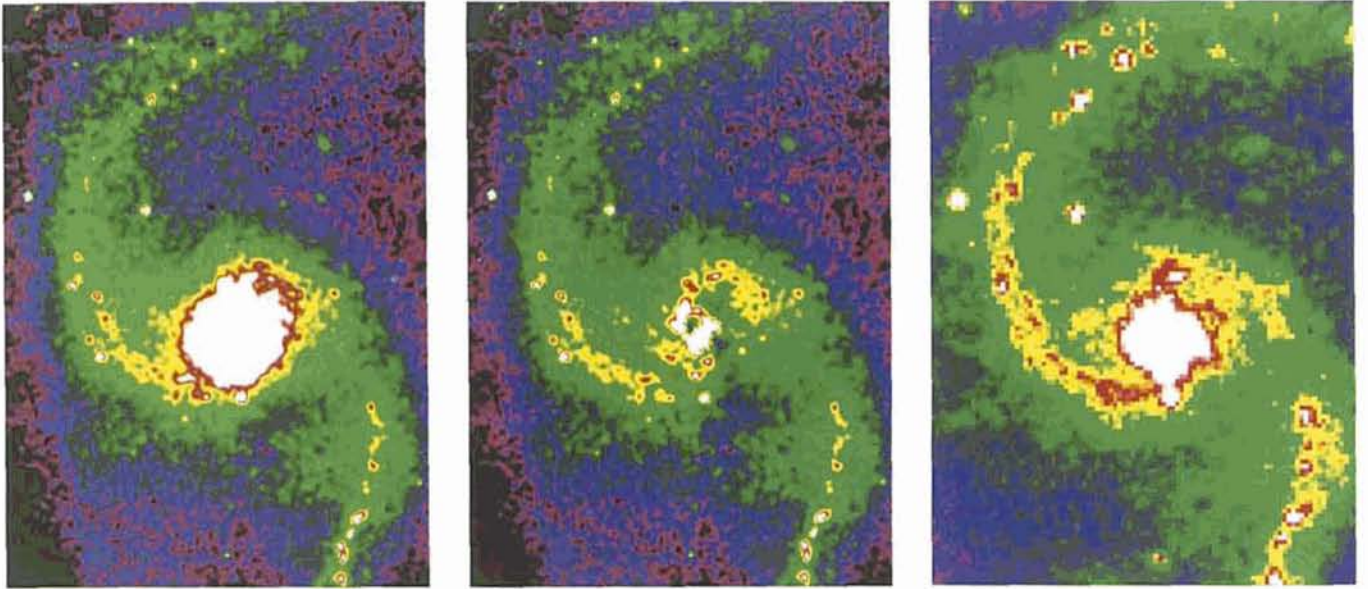


Figure 6: NGC5247. The left panel is a smoothed K' mosaic image; centre panel is the K' image after subtraction of a fit to the inner galaxy disk component and the right panel is an R -band image obtained by scanning the POSS E plate. N is down and E is to the left. The infrared images have been constructed from four 120s (10×12 s) exposures with the $0.49''/\text{pixel}$ objective on each of two overlapping fields on the galaxy and six sky exposures of the same duration offset several arcmin. from the galaxy. Only the frames showing systematic differences less than 1% were used and stars in the sky frames were fitted with gaussians and removed individually before subtraction from the object frames. Smoothing using the MIDAS adaptive filter technique was applied to enhance the visibility of low surface brightness features. Note that a spur off the northern spiral arm is only visible in the POSS R image and not K' suggesting that it is not part of the grand design density wave in the galaxy.

Table 2: NICMOS3 array detector characteristics.

| | |
|---|--|
| Format (pixels) | 256 × 256 |
| Pixel size | 40 μm |
| Cut-off wavelength | 2.5 μm |
| Bad pixels | < 1% ¹ |
| Quantum efficiency | ~0.6 (2.2 μm), 0.4 (1.25 μm) |
| Well capacity | ~10 ⁵ e |
| Dark current | ~30e/s ² |
| Read noise | ~30e |
| 1. Including a dead column in one quadrant. 2. Probably dominated by camera thermal background | |

Table 3: Overall system performance (objective C).

| Band | J | H | K' | K |
|--|------|------|------|------|
| Overall efficiency ¹ | 0.15 | 0.24 | 0.23 | 0.24 |
| Background (mag./arcsec) ² ² | 15.2 | 13.6 | 12.7 | 12.3 |
| Mag. Limits /arcsec ² (3 σ in 60s) ³ | 20.5 | 19.1 | 18.3 | 18.2 |
| Mag. Limits (3 σ in 60s/5" ap.) | 18.9 | 17.5 | 16.7 | 16.6 |
| 1. Detected photons as a fraction of those incident on the atmosphere taking into account telescope central obscuration and undersizing of the F/35 secondary. 2. Telescope temperature ~ 283K. 3. For 60s object and 60s sky scaled from differences of sky frames with integrations of 20 × 10s. | | | | |

has the advantage of cancelling any "dark current" pattern due to radiation seen through the filters and not present with the dark filter. The images reduced so far do appear to be flat within the noise and, at least in the K and K' prime filters, are better than can be obtained using sky flats. This seems to be due to the fact that sky-dark frames contain a faint ring-like structure which disappears in the object-sky images. Its outer diameter just matches the size of the array and is independent of magnification implying that it originates in or close to the detector. As yet, however, no convincing explanation for this effect has been found. The $0.27''/\text{pixel}$ objective also shows an additional ring which appears in both the sky and dome flats and whose origin is equally unclear. These effects are typically a few per cent of the mean background and are not apparent in the reduced images except in one or two cases where the background varied by large amounts during the measurement due to clouds. Although apparently not significantly affecting the overall performance, therefore, this problem still requires further investigation.

Another aspect requiring further study is the stability of the array response. The reproducibility between images and of the zero points derived from standard star observations over seven nights suggests that this is not a problem over most of the array area. Mosaics made

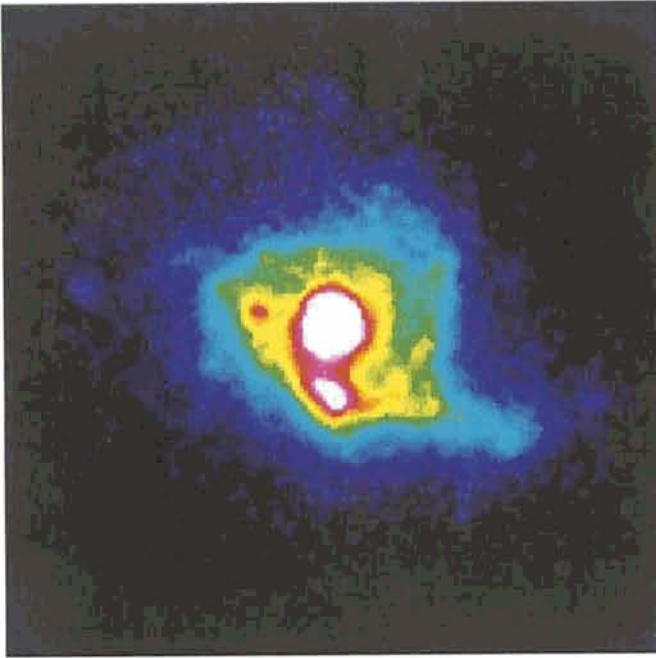


Figure 7: K' image of the merging galaxy system NGC3256. The scale is $0.27''/\text{pixel}$ and the image is the difference of single 120s ($12 \times 10\text{s}$) exposures on the galaxy and sky.

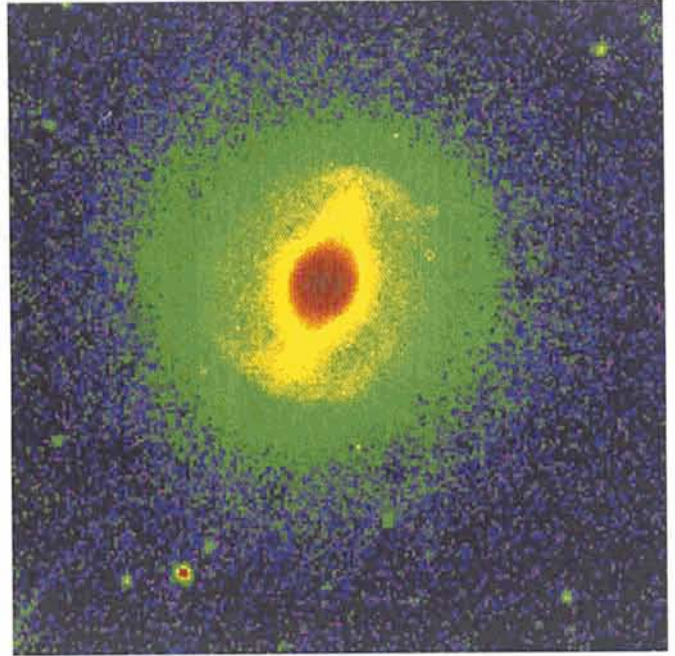


Figure 8: K' image of the Seyfert galaxy NGC3783. Scale is $0.49''/\text{pixel}$ and sky subtraction and bad pixel correction has been made using two sets of four 120s ($12 \times 10\text{s}$) exposures of the galaxy at different positions on the array and eight interleaved sky frames with the same integration time.

from overlapping images (see e.g. the RCW103 image in the June *Messenger*), however, suggest that

some instabilities at the edges could be present. These appear to be variations at the few % level and are confined to a

rather sharply defined strip along one edge. Curiously, however, this effect appears on different, orthogonal, edges in the J and K bands! Pending further investigation we assume these are intrinsic to the array (i.e. as opposed to variations in the background illumination which would be hard to explain).

4. Sample Images

A K' ($2.1 \mu\text{m}$) image of the $z = 0.2$ galaxy cluster A1689 and a narrow-band $[\text{FeII}](1.644 \mu\text{m})$ image of the supernova remnant RCW103 were already included in the June *Messenger* (68, 42) as examples of (i) "deep" imaging by combining exposures made at slightly different telescope positions and (ii) mosaicking of images displaced by almost the full field respectively. Figures 5–11 are some additional images selected to illustrate other possible modes and applications of the camera. As only single-object positions were used for most of these observations the bad pixels have generally been masked and replaced by interpolation in the surrounding area. Unless otherwise stated in the figure caption these images are oriented with N at the top and E to the left.

Conclusions

The overall measured performance of IRAC2 is close to that predicted in advance of the test and, although some aspects still require further investiga-

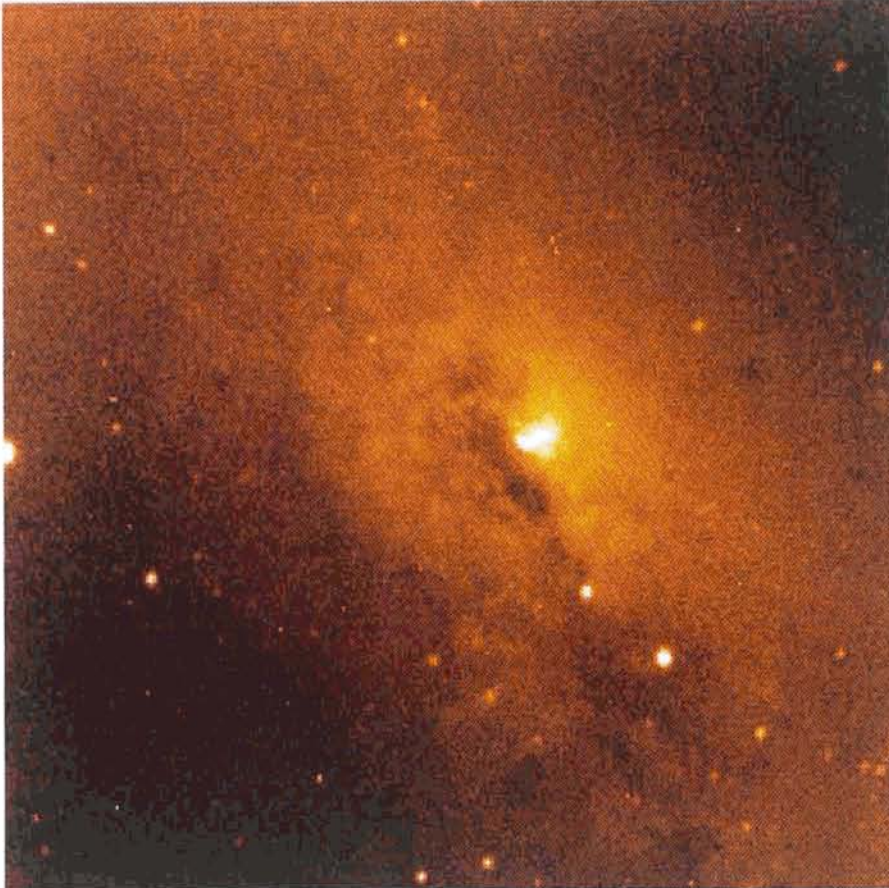


Figure 9: J image of the visually obscured nucleus in the nearly edge on galaxy NGC4945 made from three 120s ($6 \times 20\text{s}$) exposures on the galaxy and two on the sky. Scale is $0.49''/\text{pixel}$.



Figure 10: Narrow-band images of the planetary nebula NGC6302 at $0.27''/\text{pixel}$ in the [SiVI] ($1.96\ \mu\text{m}$) coronal (top), [FeII] ($1.644\ \mu\text{m}$) (middle) and Br $_{\gamma}$ ($2.16\ \mu\text{m}$) (lower) lines. The upper and lower images were obtained with the scanning Fabry Perot and are differences of images measured with the etalon centred on the line wavelength and in the adjacent continuum. The centre image was obtained with the narrow band [Fe II] filter and has been sky subtracted. The exposure time for each frame was 4 min. ($8 \times 30\text{s}$). Note the pronounced, extended, [FeII] filaments which are not present in the other lines.

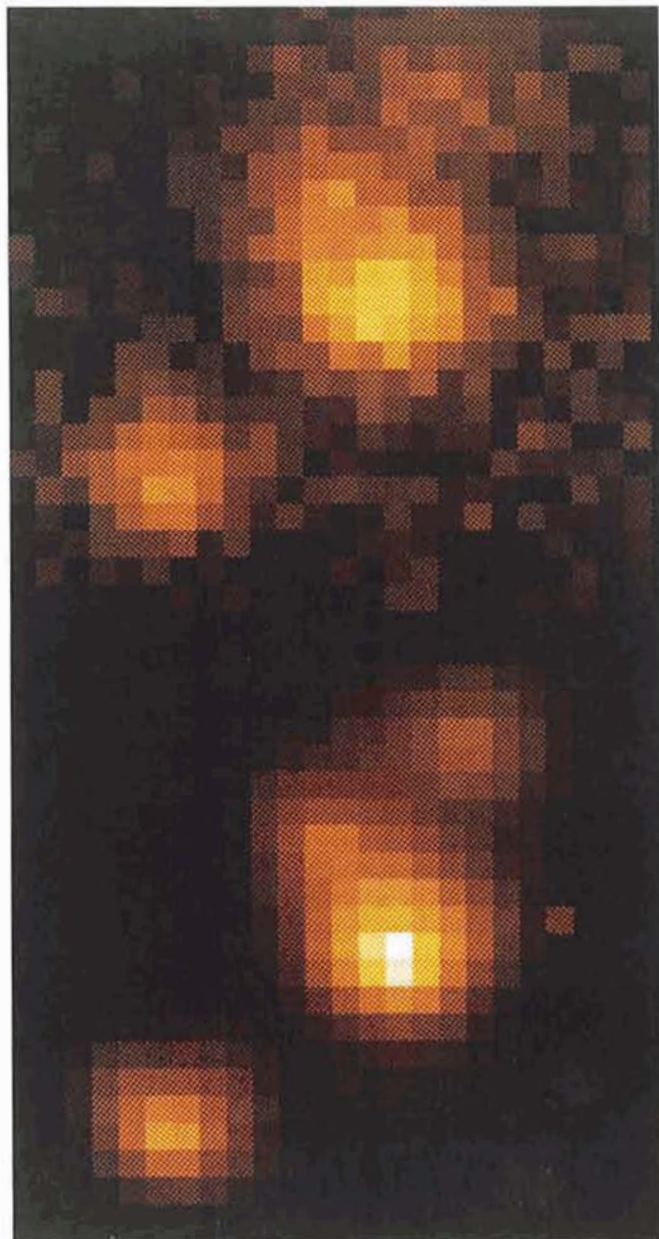


Figure 11: Example of partial seeing correction using the software shift and add feature of the multiple non-destructive read mode. The upper and lower panels show the same small region ($\sim 3.5 \times 3.5''$) of a $36 \times 36''$ K' image of the globular cluster M2 observed at $0.14''/\text{pixel}$ with and without real time application of image shifts. The integration time in both cases was 30s during which time the integration ramp was non-destructively sampled every 700 msec. In the tracked case, each difference pair of non-destructively read images was shifted by an amount corresponding to the movement of the brightest pixel in the reference star image before computing the slopes of the integration ramps.

tion, this camera already offers powerful new infrared observing opportunities on La Silla.

Acknowledgements

We are grateful to Klaus Banse for assistance in setting up the MIDAS sessions at the telescope and to Preben Grosbøl and Reynier Peletier for expert assistance with the reduction and evaluation of the test data.

“Strasbourg-ESO Catalogue of Galactic Planetary Nebulae” Available

The Catalogue which comprises 1820 objects, is divided into Part I and Part II. Part I (195 pages) contains the following subjects: A. Explanation of the Catalogue – B. Tables – C. References of papers containing 20 objects or more – D. Finding Charts, and Part II (747 pages) contains The Catalogue.

Editors are A. Acker, F. Ochsenbein, B. Stenholm, R. Tylenda, J. Marcout and C. Schohn. The price of the Catalogue is DM 135.– (prepayment required). Payments have to be made to the ESO bank account 2102002 with Commerzbank München or by cheque, addressed to the attention of ESO, Financial Services, Karl-Schwarzschild-Str. 2, D-8046 Garching bei München, Germany